LETTER

doi:10.1038/nature16463

Observation of polar vortices in oxide superlattices

A. K. Yadav[1,2*], C. T. Nelson[1,3,4*], S. L. Hsu[1,3,4], Z. Hong[5], J. D. Clarkson[1,3], C. M. Schlepütz[6], A. R. Damodaran[1], P. Shafer[7], E. Arenholz[7], L. R. Dedon[1], D. Chen[1,3], A. Vishwanath[2,3], A. M. Minor[1,2,4], L. Q. Chen[5], J. F. Scott[8], L. W. Martin[1,2] & R. Ramesh[1,2,3]

The complex interplay of spin, charge, orbital and lattice degrees of freedom provides a plethora of exotic phases and physical phenomena[1–5]. In recent years, complex spin topologies have emerged as a consequence of the electronic band structure and the interplay between spin and spin–orbit coupling in materials[6,7]. Here we produce complex topologies of electrical polarization—namely, nanometre-scale vortex–antivortex (that is, clockwise–anticlockwise) arrays that are reminiscent of rotational spin topologies[6]—by making use of the competition between charge, orbital and lattice degrees of freedom in superlattices of alternating lead titanate and strontium titanate layers. Atomic-scale mapping of the polar atomic displacements by scanning transmission electron microscopy reveals the presence of long-range ordered vortex–antivortex arrays that exhibit nearly continuous polarization rotation. Phase-field modelling confirms that the vortex array is the low-energy state for a range of superlattice periods. Within this range, the large gradient energy from the vortex structure is counterbalanced by the corresponding large reduction in overall electrostatic energy (which would otherwise arise from polar discontinuities at the lead titanate/strontium titanate interfaces) and the elastic energy associated with epitaxial constraints and domain formation. These observations have implications for the creation of new states of matter (such as dipolar skyrmions, hedgehog states) and associated phenomena in ferroic materials, such as electrically controllable chirality.

The ability to synthesize heteroepitaxial complex oxides has enabled unprecedented access to high-quality, single-crystalline materials and routes to manipulate order parameters[8,9]. In ferroelectric materials (that is, those possessing a spontaneous, switchable electrical polarization), epitaxial strain and advances in layer-by-layer growth techniques have enabled the study of the fundamental limits of ferroelectricity[10,11] and the discovery of novel interfacial phenomena[12,13]. In short-period (of only a few unit cells) superlattices of $PbTiO_3$/$SrTiO_3$, researchers observed the emergence of 'improper' ferroelectricity arising from octahedral tilts in the $SrTiO_3$ layer[14–16] and this has motivated a number of additional studies of such effects[17]. At relatively large length scales (greater than 5 nm), interfaces still play a formative role, driving both bulk[18] and thin-film[19–21] ferroelectrics to form patterns of flux-closure polar domains, whose microstructures have been the topic of extensive research including atomic-scale polarization studies[19,22,23]. At intermediate length scales (tens of unit cells), theoretical studies have suggested that there is potential for topological structures such as vortices, waves and skyrmions[24–30], depending on the interplay between strain, depolarization and gradient energies. In this work, we demonstrate ordered arrays of polar vortices, made up of vortex–antivortex pairs, in ferroelectric/paraelectric superlattices.

Symmetric $(SrTiO_3)_n/(PbTiO_3)_n$ superlattices with $n = 2$–27 were synthesized on $DyScO_3$ $(001)_{pc}$ (where pc refers to the pseudocubic notation) substrates via reflection high-energy electron diffraction (RHEED)-assisted pulsed-laser deposition (details of the growth are provided in Methods and Extended Data Fig. 1). Superlattices are henceforth referred to using the '$n \times n$' shorthand wherein n corresponds to the thickness of the $SrTiO_3$ and $PbTiO_3$ layers in unit cells (structures depicted schematically on the right of Fig. 1a). Chemical analysis via Rutherford backscattering spectrometry (RBS) confirms stoichiometric $PbTiO_3$ within the detectability limits of the technique (±1%, Extended Data Fig. 2). A typical low-magnification, scanning transmission electron microscopy (STEM, details in Methods) image of the cross-section of a 10×10 superlattice taken along the $[010]_{pc}$ zone axis reveals the layer uniformity (Fig. 1a), and atomic-scale high-resolution STEM (HR-STEM) confirms sharp and coherent interfaces (Extended Data Fig. 3a). X-ray diffraction studies including symmetric Bragg scans (Fig. 1b) and reciprocal space maps (RSMs, Fig. 1c) reveal superlattice reflections in the out-of-plane direction (L, $[001]_{pc}$) corresponding to the superlattice period of 9–10 nm. Side-lobe diffraction peaks are also observed along the in-plane direction (K, $[010]_{pc}$) corresponding to a 9–10 nm periodicity (arising from a polar ordering which is discussed in the following section).

Mapping of the atomic polar displacement ($\boldsymbol{P}_{PD}$) was performed to determine the polarization distribution within the superlattices. A displacement vector-mapping algorithm[23] (details in Methods and Extended Data Figs 3 and 4) was implemented on the cross-sectional HR-STEM images to measure local non-centrosymmetry of the lattice. A vector map of these polar displacements within a 10×10 superlattice (Fig. 2a) shows the formation of long-range, ordered arrays of vortex structures with alternating rotation directions. The lateral periodicity is approximately the same as the superlattice period (~10 nm), closely matching the in-plane (K, $[010]_{pc}$) periodicity observed in the RSMs. These vortices exhibit a continuous rotation of the local polarization vector, in contrast to segregation into uniform domains and domain walls typical of ferroelectric domain and flux-closure structures[19–21]. As a consequence, a dominant fraction of the $PbTiO_3$ layers exhibit a continual rotation of $\boldsymbol{P}_{PD}$, as illustrated in maps of the curl (that is, vorticity) of the displacement vector field $(\nabla \times \boldsymbol{P}_{PD})_{[010]}$ (Fig. 2c; additional details are provided in Methods and the full curl map corresponding to Fig. 2a is found in Extended Data Fig. 5a). To better understand the energetics of the vortex–antivortex states, we carried out phase-field modelling of the polarization structure as a function of superlattice periodicity (details in Methods). The phase-field-calculated polarization maps for the same 10×10 superlattice indicate the formation of a vortex–antivortex ground state bearing close resemblance to the experimental observations (Fig. 2d).

Both in- and out-of-plane long-range vortex ordering is observed by electron diffraction and dark-field transmission electron microscopy (DF-TEM) along cross-section and planar views (Fig. 3a and b, respectively). The cross-sectional DF-TEM images show a long-range

[1]Department of Materials Science and Engineering, University of California, Berkeley, California 94720, USA. [2]Materials Sciences Division, Lawrence Berkeley National Laboratory, Berkeley, California 94720, USA. [3]Department of Physics, University of California, Berkeley, California 94720, USA. [4]National Center for Electron Microscopy, Molecular Foundry, Lawrence Berkeley National Laboratory, Berkeley, California 94720, USA. [5]Department of Materials Science and Engineering, Pennsylvania State University, State College, Pennsylvania 16802, USA. [6]Advanced Photon Source, Argonne National Laboratory, Argonne, Illinois 60439, USA. [7]Advanced Light Source, Lawrence Berkeley National Laboratory, Berkeley, California 94720, USA. [8]Schools of Chemistry and Physics, University of St Andrews, St Andrews KY16 9ST, UK.
*These authors contributed equally to this work.

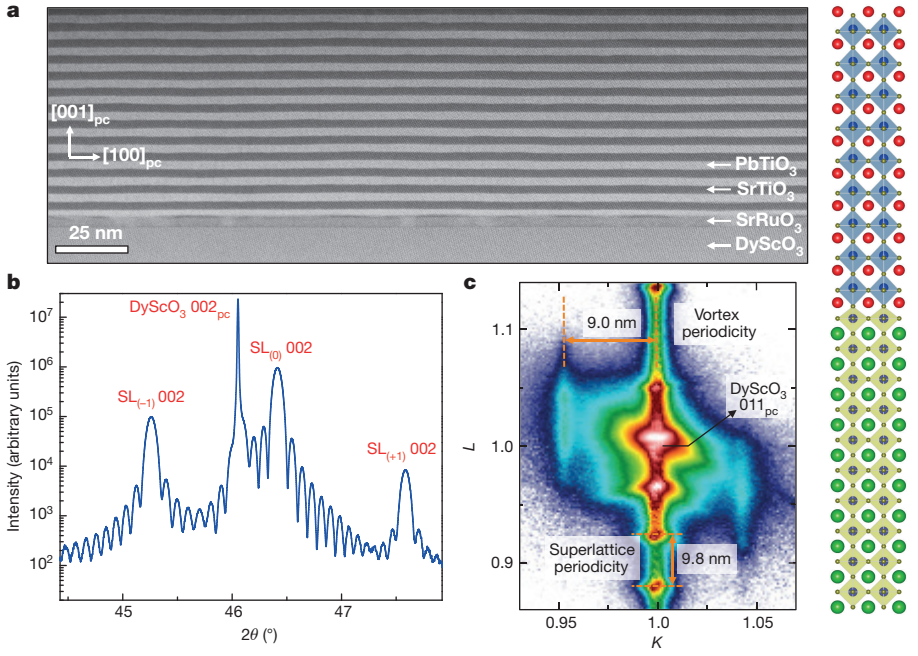

Figure 1 | Structural characterization of $(SrTiO_3)_n/(PbTiO_3)_n$ superlattices. a, Low-magnification, STEM image of the cross-section of a $(SrTiO_3)_{10}/(PbTiO_3)_{10}$ superlattice, together with a schematic illustration of the superlattice structure (right). The $PbTiO_3$ (top) is illustrated for the case of a $[001]_{pc}$ (upward) polarization which results from the downward displacement of the Ti-'centred' oxygen octahedra relative to Pb (red, blue, green and gold spheres indicate Pb, Ti, Sr and O atoms, respectively; blue- and green-shaded regions surrounding Ti atoms show oxygen octahedra). **b**, High-resolution θ-2θ symmetric scan of a 100-nm $(SrTiO_3)_{10}/(PbTiO_3)_{10}$ superlattice showing the presence of *Pendellösung* fringes, which attest to the smoothness of the surface and the high quality of the 100-nm-thick superlattices (see Methods for details and nomenclature used for peak labels). **c**, Synchrotron-based, in-plane X-ray RSM study of a $(SrTiO_3)_{12}/(PbTiO_3)_{12}$ superlattice about the $DyScO_3$ 011_{pc} diffraction condition. The asymmetric L–K scan reveals satellite peaks corresponding to vortex–antivortex pairs with ~10 nm periodicity.

periodic array of intensity modulation which corresponds to the vortex–antivortex pairs with a spacing of 9–10 nm both in and out of the plane of the superlattice. Like the X-ray RSM studies, the long-range order also manifests as additional superlattice reflections in the selected-area electron diffraction (SAED) patterns in both cross-section and planar views (see the magnified $00\bar{1}_{pc}$ and $0\bar{5}0_{pc}$ reflections from the SAED patterns in Fig. 3a inset and Fig. 3b inset, respectively). The uniform array of stripes in the planar-view DF-TEM (Fig. 3b), again with a 9–10 nm periodicity, suggests that the vortices extend over distances of at least 1 μm. We also note that vortices are observed to exist in both in-plane directions (Extended Data Fig. 6).

Phase-field modelling of the $PbTiO_3/SrTiO_3$ superlattices was performed to study the energetics and to ascertain the 3D structure of the vortex–antivortex pairs. A range of symmetric superlattice periodicities were simulated, allowing each to evolve from a random initial state according to the time-dependent Ginzburg–Landau equation (details in Methods). The 3D structure of the 10×10 superlattice, corresponding to our experimental HR-STEM studies, is shown in Fig. 4. With no a priori assumption of the polarization ($\boldsymbol{P}$) distribution, the model converges to a vortex–antivortex array structure. For comparison, sub-regions of the HR-STEM and planar-view DF-TEM images are projected on the same 3D axes as the model (Fig. 4). The tubular, ordered vortices match the experimentally observed structures closely. The polarization rotation extracted from the model is mapped onto the front plane and in 3D isosurfaces (Fig. 4) using a blue/red colour scale corresponding to alternating clockwise (vortices) and anticlockwise (antivortices) according to the $(\nabla \times \boldsymbol{P})_{[010]}$ curl of the polarization. Two additional slices through the 3D structure show the component of polarization along $[100]_{pc}$ ($\boldsymbol{P}_{[100]}$) and $[001]_{pc}$ ($\boldsymbol{P}_{[001]}$). Like the polar displacements from the HR-STEM, the model lacks discrete domains and, instead, exhibits a smooth rotation of the polarization. The long-range order is also in good agreement, preferring interlayer alignment of the vortices, particularly with matching rotation directions (Extended Data Fig. 5c).

On the basis of both the experimental results and the phase-field simulations, the observed vortex structure results (primarily) from competition between three energies. The first is the elastic energy, which arises from the fact that the $PbTiO_3$ is epitaxially constrained (in a tensile fashion) by the $DyScO_3$ substrate which traditionally drives the $PbTiO_3$

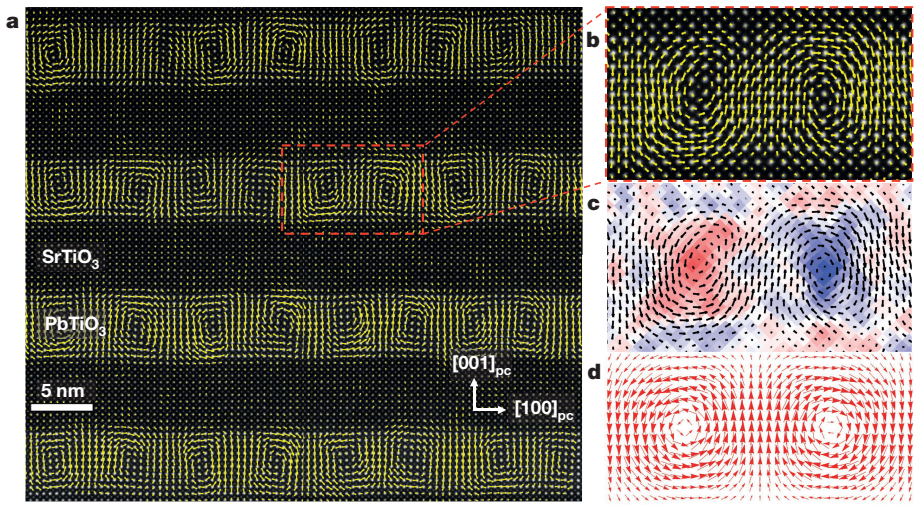

Figure 2 | Observation of vortex–antivortex structures. a, Cross-sectional HR-STEM image with an overlay of the polar displacement vectors ($\boldsymbol{P}_{PD}$, indicated by yellow arrows) for a $(SrTiO_3)_{10}/(PbTiO_3)_{10}$ superlattice, showing that an array of vortex–antivortex pairs is present in each $PbTiO_3$ layer. **b**, A magnified image of a single vortex–antivortex pair, showing the full density of data points (one for each atom) and the continuous rotation of the polarization state within such vortex–antivortex pairs. **c**, The curl of the polar displacement $(\nabla \times \boldsymbol{P}_{PD})_{[010]}$ for the same vortex–antivortex pair reveals the alternating rotation directions of the structures (see details in Methods and Extended Data Fig. 5a and b). The $(\nabla \times \boldsymbol{P}_{PD})_{[010]}$ curl value is plotted with a red/blue colour scale where no-vorticity (curl = 0) is white, clockwise (negative) is blue and anticlockwise (positive) is red. **d**, Polarization vectors from a phase-field simulation of the same $(SrTiO_3)_{10}/(PbTiO_3)_{10}$ superlattice, which predicts vortex–antivortex pairs that closely match the experimental observations.

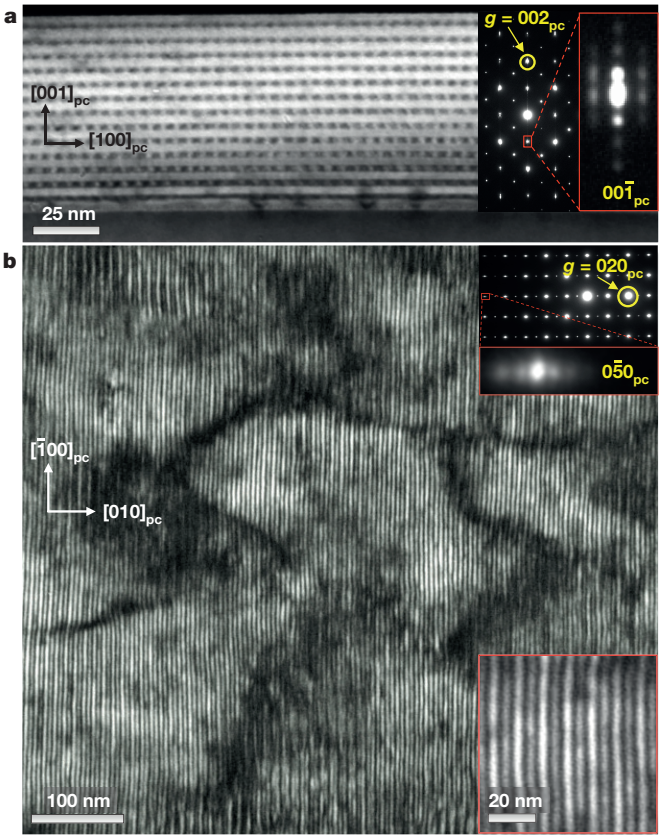

Figure 3 | Long-range ordering of vortices. a, Main panel, cross-sectional DF-TEM images of a $(SrTiO_3)_{10}/(PbTiO_3)_{10}$ superlattice revealing long-range ordering of vortices (each bright/dark modulation corresponds to a period of the vortex–antivortex structure). Inset, SAED pattern for the sample with the *g*-vector of the two-beam imaging condition indicated by the yellow arrow. Close inspection of the SAED pattern reveals superlattice reflections both in and out of the plane, suggesting long-range ordering of the vortex structures (boxed area of inset with $00\bar{1}_{pc}$ reflection is shown magnified at right). **b**, Planar-view DF-TEM imaging of a $(SrTiO_3)_{16}/(PbTiO_3)_{16}$ superlattice which likewise exhibits long-range in-plane ordering associated with the vortex–antivortex pairs along $[\bar{1}00]_{pc}$ and confirms the widespread occurrence of these vortex pairs in the superlattice films. The upper inset shows the SAED pattern for the sample with the *g*-vector of the two-beam imaging condition indicated by the yellow arrow. Again, close inspection of the diffraction pattern (boxed area of inset shown magnified) reveals in-plane superlattice reflections indicating long-range ordering of the vortex structures. The lower inset shows a magnified view of the vortex structures, again revealing ~10 nm periodicities.

to adopt a mixture of in-plane $\boldsymbol{P}_{[100]/[010]}$ and out-of-plane $\boldsymbol{P}_{[001]}$ polarizations (that is, a *c*/*a* domain structure). The second major contribution is electrostatic energy from built-in electric fields. As one transitions from the $PbTiO_3$ to the $SrTiO_3$ layer there is likely to be a large polar discontinuity normal to the interface and thus there is a strong driving force for bound charges since $\nabla \cdot \boldsymbol{P} \neq 0$. Finally, the third major energy in competition is the gradient energy. This is the energy required to rotate or change the direction or magnitude of the polarization. All told, in this system, these three energies combine to create a new topology of polarization—the system localizes the in-plane $\boldsymbol{P}_{[100]/[010]}$ components at the $PbTiO_3/SrTiO_3$ interfaces and forms alternating out-of-plane $\boldsymbol{P}_{[001]}$ components mid-layer—thereby creating a rotating polarization.

It should also be noted that the balance of these terms, and thus the ground-state structure, is strongly dependent on the superlattice period. In short-period superlattices ($n < 10$), the vortex becomes unstable and, instead, the $PbTiO_3$ minimizes the electrostatic and gradient energy at the expense of elastic energy by adopting only in-plane $\boldsymbol{P}_{[100]/[010]}$ components (that is, a_1/a_2 domain structures). As the superlattice period increases to intermediate length scales, a discontinuity in the total energy appears in the phase diagram (derived from the phase-field simulations and total energy calculations) and thus a co-existence of the a_1/a_2 and vortex–antivortex structures is observed. In long-period superlattices ($n \gtrsim 18$), the system begins to evolve into classical flux-closure domain structures characterized by the formation of discrete domains surrounding localized polarization gradients at domain walls. A side-by-side comparison of HR-STEM polar displacement maps and phase-field

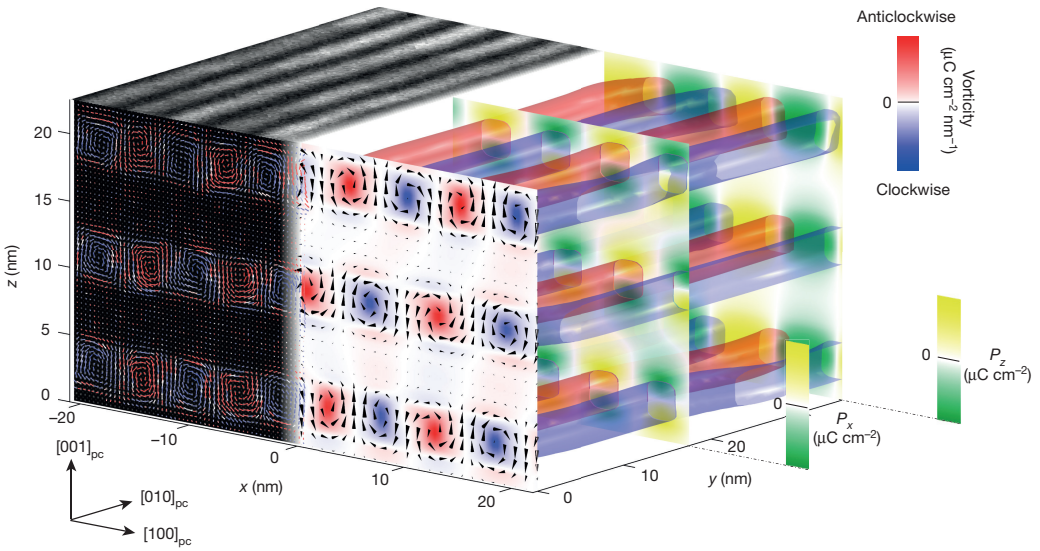

Figure 4 | Three-dimensional phase-field simulation for a $(SrTiO_3)_{10}/(PbTiO_3)_{10}$ superlattice. The 3D geometry of the vortex–antivortex array from phase-field simulation of a $(SrTiO_3)_{10}/(PbTiO_3)_{10}$ superlattice is shown on the right. The front cross-section of the model shows the polarization vector $\boldsymbol{P}$ ordered into clockwise (blue) and anticlockwise (red) vortex–antivortex states which extend along the $[010]_{pc}$. For comparison, on the left is shown a cross-sectional HR-STEM image overlaid with a polar displacement vector map and a planar-view DF-TEM image projected onto the front and top planes of the axes, respectively. Red/blue colour scales correspond to the curl of the polarization extracted from the phase-field model and the HR-STEM polar displacement map ($\boldsymbol{P}_{PD}$). The scale bars on P_x and P_z are from −44.81 to 44.81 (μC cm^{-2}) and from −54.24 to 54.24 (μC cm^{-2}), respectively, whereas the vorticity is from −129.36 to 129.36 (μC cm^{-2} nm^{-1}).

simulations for vortex (10×10) and flux-closure (50×50) structures is provided (Extended Data Fig. 7); we also show the superlattice-period-dependent evolution of structures from phase-field models (Extended Data Fig. 8). In summary, the continuous curling of polarization allows the simultaneous achievement of electrostatically favoured, non-diverging polarization and a strain-favoured mixture of in-plane and out-of-plane components of polarization, stabilizing novel vortex states.

These observations beget several important questions and avenues for future exploration. First, the vortices are observed to be slightly asymmetric (the cores not being perfectly centred and equidistant, Fig. 2a), which could be a source of chirality and potentially used to produce tunable optical behaviour. Second, although the long-range, in-plane order of the vortex structures is quite robust, the out-of-plane order is somewhat less so. This out-of-plane ordering is likely to be a low-energy excitation (akin to ferroelectric liquid crystals and Abrikosov lattices in superconductors) and consequently to exhibit a certain degree of disorder and the potential for multiple ground states, which may be a rich area for exploration of the macro-scale ordering by tuning the interlayer stacking. Last, the generation of vortex topologies could be extended to other material systems and other symmetries—for example, a multiferroic $BiFeO_3$ system could also provide the possibility of enhancing the canted moment arising from Dzyaloshinski–Moriya interactions.

Online Content Methods, along with any additional Extended Data display items and Source Data, are available in the online version of the paper; references unique to these sections appear only in the online paper.

Received 17 June; accepted 16 November 2015.
Published online 27 January 2016.

1. Tokura, Y. & Nagaosa, N. Orbital physics in transition-metal oxides. *Science* **288,** 462–468 (2000).
2. Imada, M., Fujimori, A. & Tokura, Y. Metal-insulator transitions. *Rev. Mod. Phys.* **70,** 1039–1263 (1998).
3. Zubko, P. *et al.* Interface physics in complex oxide heterostructures. *Annu. Rev. Condens. Matter Phys.* **2,** 141–165 (2011).
4. Millis, A. J. Lattice effects in magnetoresistive manganese perovskites. *Nature* **392,** 147–150 (1998).
5. Kivelson, S. A., Fradkin, E. & Emery, V. J. Electronic liquid-crystal phases of a doped Mott insulator. *Nature* **393,** 550–553 (1998).
6. Nagaosa, N. & Tokura, Y. Topological properties and dynamics of magnetic skyrmions. *Nature Nanotechnol.* **8,** 899–911 (2013).
7. Schulz, T. *et al.* Emergent electrodynamics of skyrmions in a chiral magnet. *Nature Phys.* **8,** 301–304 (2012).
8. Schlom, D. G. *et al.* Strain tuning of ferroelectric thin films. *Annu. Rev. Mater. Res.* **37,** 589–626 (2007).
9. Mannhart, J. & Schlom, D. G. Oxide interfaces — an opportunity for electronics. *Science* **327,** 1607–1611 (2010).
10. Dawber, M., Rabe, K. M. & Scott, J. F. Physics of thin-film ferroelectric oxides. *Rev. Mod. Phys.* **77,** 1083–1130 (2005).
11. Fong, D. D. *et al.* Ferroelectricity in ultrathin perovskite films. *Science* **304,** 1650–1653 (2004).
12. Chakhalian, J., Millis, A. J. & Rondinelli, J. Whither the oxide interface. *Nature Mater.* **11,** 92–94 (2012).
13. Yu, P. Interface control of bulk ferroelectric polarization. *Proc. Natl Acad. Sci. USA* **109,** 9710–9715 (2012).
14. Bousquet, E. *et al.* Improper ferroelectricity in perovskite oxide artificial superlattices. *Nature* **452,** 732–736 (2008).
15. Sichuga, D. *et al.* Chiral patterns of tilting of oxygen octahedra in zero-dimensional ferroelectrics and multiferroics: a first principle-based study. *Phys. Rev. Lett.* **104,** 207603 (2010).
16. Zhao, H. J. *et al.* Atomistic theory of hybrid improper ferroelectricity in perovskites. *Phys. Rev. B* **89,** 174101(R) (2014).
17. Pitcher, M. J. *et al.* Tilt engineering of spontaneous polarization and magnetization above 300K in a bulk layered perovskite. *Science* **347,** 420–424 (2015).
18. McQuaid, R. G. P., McGilly, L. J., Sharma, P., Gruverman, A. & Gregg, J. M. Mesoscale flux-closure domain formation in single-crystal $BaTiO_3$. *Nature Commun.* **2,** 404 (2011).
19. Tang, Y. L. *et al.* Observation of periodic array of flux-closure quadrants in strained ferroelectric $PbTiO_3$ films. *Science* **348,** 547–551 (2015).
20. Gruverman, A. *et al.* Vortex ferroelectric domains. *J. Phys. Condens. Matter* **20,** 342201 (2008).
21. Balke, N. *et al.* Enhanced electric conductivity at ferroelectric vortex cores in $BiFeO_3$. *Nature Phys.* **8,** 81–88 (2012).
22. Jia, C.-L., Urban, K. W., Alexe, M., Hesse, D. & Vrejoiu, I. Direct observation of continuous electric dipole rotation in flux-closure domains in ferroelectric $Pb(Zr, Ti)O_3$. *Science* **331,** 1420–1423 (2011).
23. Nelson, C. T. *et al.* Spontaneous vortex nanodomain arrays at ferroelectric heterointerfaces. *Nano Lett.* **11,** 828–834 (2011).
24. Naumov, I. I., Bellaiche, L. & Fu, H. Unusual phase transitions in ferroelectric nanodisks and nanorods. *Nature* **432,** 737–740 (2004).
25. Choudhury, N., Walizer, L., Lisenkov, S. & Bellaiche, L. Geometric frustration in compositionally modulated ferroelectrics. *Nature* **470,** 513–517 (2011).
26. Ponomareva, I., Naumov, I. & Bellaiche, L. Low-dimensional ferroelectrics under different electrical and mechanical boundary conditions: atomistic simulations. *Phys. Rev. B* **72,** 214118 (2005).
27. Prosandeev, S. & Bellaiche, L. Characteristics and signatures of dipole vortices in ferroelectric nanodots: first-principles-based simulations and analytical expressions. *Phys. Rev. B* **75,** 094102 (2007).
28. Prosandeev, S., Ponomareva, I., Naumov, I., Kornev, I. & Bellaiche, L. Original properties of dipole vortices in zero-dimensional ferroelectrics. *J. Phys. Condens. Matter* **20,** 193201 (2008).
29. Sichuga, D. & Bellaiche, L. Epitaxial $Pb(ZrTi)O_3$ ultrathin films under open circuit electrical boundary conditions. *Phys. Rev. Lett.* **106,** 196102 (2011).
30. Levanyuk, A. P. & Blinc, R. Ferroelectric phase transitions in small particles and local regions. *Phys. Rev. Lett.* **111,** 097601 (2013).

Acknowledgements A.K.Y. and R.R. acknowledge support from the Office of Basic Energy Sciences, US Department of Energy (DE-AC02-05CH11231), for the synthesis and characterization of superlattices. R.R. and C.T.N. acknowledge support from the Office of Basic Energy Sciences, US Department of Energy (DE-AC02-05CH11231), for TEM characterization of superlattices. S.L.H. acknowledges support from the National Science Foundation under the MRSEC program (DMR-1420620). Z.H. acknowledges support from the National Science Foundation (DMR-1210588). J.D.C. acknowledges support from the Office of Basic Energy Sciences, US Department of Energy (DE-AC02-05CH11231). C.M.S. acknowledges use of the Advanced Photon Source, which was supported by the US Department of Energy, Office of Science, Office of Basic Energy Science (DE-AC02-06CH11357), for the synchrotron-based reciprocal space map studies of superlattice structures at Sector 33-BM-C beamline. A.R.D. acknowledges support from the Army Research Office (W911NF-14-1-0104). P.S. and E.A. acknowledge support from the Director, Office of Science, Office of Basic Energy Sciences, US Department of Energy (DE-AC02-05CH11231), for the synchrotron-based studies of the superlattice structures. L.R.D. acknowledges support from the US Department of Energy, Office of Basic Energy Sciences (DE-SC0012375) for the chemical analysis of the superlattice structures. D.C. acknowledges support from the National Science Foundation under the MRSEC program (DMR-1420620). A.V. and A.M.M. acknowledge support from Office of Basic Energy Sciences, US Department of Energy (DE-AC02-05CH11231). L.Q.C. acknowledges support from the National Science Foundation (DMR-1210588). L.W.M. acknowledges support from the National Science Foundation (DMR-1451219). Electron microscopy of superlattice structures was performed at the Molecular Foundry, LBNL, supported by the Office of Science, Office of Basic Energy Sciences, US Department of Energy (DE-AC02-05CH11231). Z.H. thanks J. Britson, F. Xue and J. Wang for help and discussions.

Author Contributions A.K.Y. and R.R. designed the experiments. A.K.Y. carried out the synthesis and characterization of superlattice samples. C.T.N. and S.L.H. performed TEM characterization of superlattice samples, along with the detailed polarization vector analysis. Z.H. performed phase-field calculations for these superlattices. C.M.S. did the reciprocal space map studies of superlattice structures using synchrotron X-ray diffraction. L.R.D did the chemical analysis of the superlattice films using Rutherford backscattering. D.C., J.D.C. and A.R.D. did the piezoforce microscopy studies of superlattice films. P.S. and E.A. did synchrotron X-ray circular dichroism measurements on superlattice films. R.R., L.W.M., A.K.Y., C.T.N., A.R.D., J.D.C., Z.H., L.Q.C., A.V. and J.F.S. analysed the data and co-wrote the manuscript. R.R., L.W.M., A.M.M. and L.Q.C. supervised the research. All authors contributed to the discussions and manuscript preparation.

Author Information Reprints and permissions information is available at www.nature.com/reprints. The authors declare no competing financial interests. Readers are welcome to comment on the online version of the paper. Correspondence and requests for materials should be addressed to R.R. (rramesh@berkeley.edu).

METHODS

Material system. The materials used in this study are lead titanate ($PbTiO_3$), strontium titanate ($SrTiO_3$), strontium ruthenate ($SrRuO_3$) and dysprosium scandate ($DyScO_3$). $PbTiO_3$ has a tetragonal structure with space group $P4mm$ and bulk lattice parameters[31] $a = 3.904$ Å and $c = 4.178$ Å. $PbTiO_3$ is a ferroelectric at room temperature with an axis of spontaneous polarization along [001] and undergoes a phase transition[31] from a tetragonal (ferroelectric) to a cubic (paraelectric) structure at 490 °C in the bulk. $SrTiO_3$, on the other hand, is a band insulator at room temperature with a cubic structure having a bulk lattice parameter of $a = 3.905$ Å and space group $Pm\bar{3}m$. $SrRuO_3$ is a ferromagnetic metal at room temperature with an orthorhombic structure having space group $Pbnm$ and bulk lattice parameters[32] of $a = 5.567$ Å, $b = 5.530$ Å and $c = 7.845$ Å. $DyScO_3$ is a band insulator at room temperature and has an orthorhombic structure with space group $Pbnm$ and bulk lattice parameters[33] of $a = 5.440$ Å, $b = 5.717$ Å and $c = 7.903$ Å. The orientation between the pseudocubic indices used in the text and the orthorhombic indices of the $DyScO_3$ substrate are $(001)_{pc} \| (110)_O$, $(100)_{pc} \| (\bar{1}10)_O$, $(010)_{pc} \| (001)_O$.

Synthesis of the superlattices using RHEED-assisted pulsed-laser deposition. Superlattices of $(SrTiO_3)_n/(PbTiO_3)_n$ were synthesized on 5 nm $SrRuO_3$-buffered, single crystalline $DyScO_3$ $(001)_{pc}$ substrates via pulsed-laser deposition. The growth temperature and oxygen pressure for the growth of the superlattices was 630 °C and 100 mtorr, respectively, to ensure stoichiometric transfer of both $PbTiO_3$ and $SrTiO_3$. Growth of the $SrRuO_3$ was accomplished at a growth temperature of 700 °C and an oxygen pressure of 50 mtorr. All depositions were performed at a laser fluence of 1.5 J cm^{-2}. The growth was monitored using reflection high-energy electron diffraction (RHEED) to ensure maintenance of a layer-by-layer growth mode throughout the growth process (Extended Data Fig. 1) which, in turn, enables controlled growth of the superlattices with different period-thicknesses while achieving the same total thickness. The RHEED oscillations were monitored for specular spots along $[100]_{pc}$ of the $DyScO_3$ $(001)_{pc}$ substrate. After the growth, the samples were cooled to room temperature in 50 torr of oxygen to promote full oxidation. The use of a $Pb_{1.2}TiO_3$ target was found to be critical in enabling persistent layer-by-layer growth (evidenced by RHEED oscillations obtained throughout the entire growth process, Extended Data Fig. 1), whereas the use of a stoichiometric $PbTiO_3$ target resulted in rapid transition to 3D (island) growth.

Structural characterization. *Laboratory-based X-ray diffraction.* Superlattices were characterized with a Panalytical X'Pert Pro X-ray Diffraction (XRD) machine with a Cu source. Symmetric XRD scans (Fig. 1b) were extensively performed to fully characterize the structural order in the out-of-plane direction, $[001]_{pc}$, in these superlattice structures. The superlattice period achieved via RHEED-controlled growth was later confirmed using high-resolution θ-2θ symmetric XRD scans (see, for example, Fig. 1b). The presence of thickness fringes (*Pendellösung* fringes) around both the central Bragg peak ($SL_{(0)}$ 002) and the superlattice peaks ($SL_{(-1)}$ 002 and $SL_{(+1)}$ 002) are clearly visible in 10×10 superlattices (Fig. 1b) and attest to the high crystallinity of the films, the precise nature of the interfaces, and the overall smoothness of these structures.

Synchrotron X-ray diffraction. This was employed to study the structure (both in and out of the plane) of the superlattices. The diffraction studies were performed at the Sector 33-BM-C beamline of the Advanced Photon Source, Argonne National Laboratory. The high flux from a synchrotron source delivered at this beamline was optimal for extracting lattice modulations associated with these vortex–antivortex pairs. In order to obtain a highly monochromatic beam with negligible higher-order harmonics, a double crystal monochromator in conjunction with two mirrors was used. Moreover, excellent accuracy of a Huber 4-circle diffractometer in combination with a PILATUS 100K pixel detector allowed us to determine the orientation of the crystal reliably and obtain 3D RSMs with high accuracy. The X-ray wavelength used for obtaining the RSMs was 0.8 Å ($E = 15.5$ keV).

Chemical analysis by RBS. This was employed to confirm the stoichiometry of the $PbTiO_3$ at the optimized growth conditions and to eliminate any spurious effects of non-stoichiometry on the observation of these vortex structures. The results for a 200 nm $PbTiO_3$ film are provided (Extended Data Fig. 2). These results and the corresponding fit to the data confirm the chemical composition and homogeneity of the films within the limits of experimental errors. The spectra were taken with a 3.04 MeV He ion beam incident at an angle of 22.5° relative to the sample normal. The backscattered He ions were collected by a silicon surface-barrier detector positioned at 168° with respect to the incident beam. The SIMNRA software package was used to simulate the RBS spectra and obtain the composition of the film. R^2 analysis was performed about the Pb and Ti peaks to avoid artificially increasing the value of R^2 with the inclusion of substrate peaks. R^2 was calculated using $R^2 = 1 - \frac{\sum (e_i - f_i)^2}{\sum (e_i - \bar{e})^2}$, where e_i and f_i values correspond to experimental and simulated data points, respectively, for different channel energies (indicated by variable i), and $\bar{e}$ indicates the mean of experimental data points.

Conventional and scanning transmission electron microscopy. TEM samples were prepared by mechanical polishing on an Allied High Tech Multiprep. Cross-sectional samples were polished at a 0.5° wedge, and planar samples with a flat polish. Samples were subsequently Ar ion milled using a Gatan Precision Ion Milling System with starting energies of 4 keV stepped down to a final cleaning energy of 200 eV.

Diffraction contrast TEM (Fig. 3) was performed on a JEOL 3010 at 300 kV. Dark field imaging was performed in the two-beam condition, the diffracted beam travelling along the optical axis of the TEM. The samples were tilted off zone-axis to isolate selected crystallographic planes used for imaging: $g = 002_{pc}$ for Fig. 3a and Extended Data Fig. 6a; $g = 020_{pc}$ for Figs 3b and 4; and $g = 00\bar{2}_{pc}$ for Extended Data Fig. 6b. The tilt condition used for Fig. 3a and Extended Data Fig. 6b is shown by the SAED pattern (inset) in the latter. SAED patterns inset in Fig. 3a and b were collected along the zone axis.

Scanning TEM was performed on a Cs-corrected TEAM0.5 FEI Titan microscope at 300 kV using a high-angle annular detector resulting in 'Z-contrast' images. Raster distortion was minimized using a pair of HR-STEM images of the same region taken with orthogonal scan orientations. These were used to calculate a corrected 'pre-distortion' image to minimize the slow scan axis errors[34].

Determination and mapping of the polar atomic displacements ($\boldsymbol{P}_{PD}$) was performed on the corrected HR-STEM HAADF images (Extended Data Fig. 3a, b) using local A- and B-site sublattice offset measurements[23]. The rationale is that for many displacive perovskite ferroelectrics the electric dipole moment is manifested by relative shifts of the cations, as is the case for $PbTiO_3$, and this offset can be used to infer the full polarization ($\boldsymbol{P}$). This is very helpful since the anions (oxygen) needed to fully characterize an electric dipole have relatively weak electron scattering resulting in low signal-to-noise ratio, especially for HAADF images. In room-temperature bulk $PbTiO_3$, the Ti B-site is offset by 16.2 pm and the oxygen by 47–49 pm relative to the Pb lattice in the direction opposite to the polarization[35]. Thus, we use the Ti to infer the offset of the Ti-'centred' oxygen octahedra for defining the electric dipole. Displacement vectors ($\boldsymbol{P}_{PD}$) corresponding to local offsets between the A- and B-site sublattices were calculated by first determining atomic positions by fitting each atom site in the image to four-parameter, spherical Gaussians using a trust-region algorithm in Matlab (see illustration in Extended Data Fig. 3c). Fits were performed simultaneously for five-atom clusters of the B-site-centred perovskite unit cell (Extended Data Fig. 3d). The displacement for each atom was then calculated as the difference between its atom position and the mean position (that is, centre of mass) of the surrounding four opposite-type cations (Extended Data Fig. 4c, d). Using a pseudocubic grid indexing (A-sites defining a grid) and defining the cross-section image to lie in the x–z Cartesian plane ($x = [100]_{pc}$, $z = [001]_{pc}$), for an atom at grid position i, j this corresponds to mean neighbour positions (MNP) of:

$$\mathrm{MNP}x_{ij} = (x_{i-0.5,j-0.5} + x_{i-0.5,j+0.5} + x_{i+0.5,j+0.5} + x_{i+0.5,j-0.5})/4$$

$$\mathrm{MNP}z_{ij} = (z_{i-0.5,j-0.5} + z_{i-0.5,j+0.5} + z_{i+0.5,j+0.5} + z_{i+0.5,j-0.5})/4$$

Illustrative examples for both A-site and B-site regions are shown in Extended Data Fig. 4. To maintain a consistent displacement vector sign, we reverse the order for A-sites and B-sites such that:

$$\boldsymbol{P}_{\mathrm{PD},ij\ \text{A-site}} = (x_{ij} - \mathrm{MNP}x_{ij})\hat{x} + (z_{ij} - \mathrm{MNP}z_{ij})\hat{z}$$

$$\boldsymbol{P}_{\mathrm{PD},ij\ \text{B-site}} = (\mathrm{MNP}x_{ij} - x_{ij})\hat{x} + (\mathrm{MNP}z_{ij} - z_{ij})\hat{z}$$

(as illustrated in Extended Data Fig. 4d). This convention defines a displacement vector direction nominally parallel to the full electrical polarization of the bulk crystal structure. Noise in the displacement vector fields was reduced by weighted smoothing of the first derivative over a local range of 12 atoms (calculation details below).

A conservative estimation of the experimental error in the polar displacement maps for the data set in this work was performed by statistical analysis of the distribution of the polar displacements within the $SrTiO_3$ layers. $\boldsymbol{P}_{PD}$ for the Sr and Ti atoms within the $SrTiO_3$ layers (excluding the interfaces) has an $\sigma_{RMS} = 4.88$ pm. This represents an upper bound on the experimental error, as it is predicated on all measured non-centrosymmetric distortions of $SrTiO_3$ being the result of noise. Any actual distortions, be they induced by the $PbTiO_3$ epitaxy or resulting from defects, are falsely included in this estimate.

The curl vector (or vorticity) of the displacement vector field $\boldsymbol{P}_{PD}$ in the TEM plane is the y component of $\nabla \times \boldsymbol{P}_{PD}$, or $\left(\frac{\partial P_{PD,z}}{\partial x} - \frac{\partial P_{PD,x}}{\partial z}\right)\hat{y}$ (again the TEM image is defined as the x–z plane, y is the direction of the electron beam). The polarization gradient terms $\frac{\partial P_{PD,z}}{\partial x}$ and $\frac{\partial P_{PD,x}}{\partial z}$ were calculated by a weighted least-squares fit of a two-variable (x and z) first-order polynomial to $P_{PD,x}$ and $P_{PD,z}$ at each atom site

with a fit area extending to 12 surrounding atoms. More succinctly, the local $P_{PD,x}$ and $P_{PD,z}$ values were fitted as a plane, and the derivatives are taken as the x and z slopes of the plane. A Gaussian function with a σ of the mean grid spacing was used as the weighting function, that is, the central atom was given a weight of 1 and decreased to a weight of ~0.1 for the most distant of the 12 neighbour atoms considered. The polynomial fit was used as a smoothing function for the vector fields displayed in the figures, effectively smoothing the first derivative, and the gradients input into the curl equation. The curl vectors calculated and smoothed in this manner for the HAADF image in Fig. 2 are shown in Extended Data Fig. 9a for all atom positions. A comparison between the smoothed and raw polar displacements for one of the vortices is shown in Extended Data Fig. 9b and d, respectively.

Phase-field simulations for superlattice structures. In the phase-field modelling of the superlattice films, the evolution of the polarization was obtained by solving the time-dependent Ginzburg-Landau (TDGL) equations:

$$\frac{\partial P_i(\boldsymbol{r},t)}{\partial t} = -L\frac{\delta F}{\delta P_i(\boldsymbol{r},t)}(i=1,2,3) \quad (1)$$

where L, $\boldsymbol{r}$, and t denote the kinetic coefficient, spatial position vectors, and time, respectively. The contributions to the total free energy F include the Landau bulk energy, elastic energy, electric (electrostatic) energy, and gradient energy, that is:

$$F = \int \left(f_{\text{Landau}} + f_{\text{elastic}} + f_{\text{electric}} + f_{\text{gradient}}\right) \mathrm{d}V \quad (2)$$

The expression of each energy density can be found in the literature[36–38]. Owing to the inhomogeneity of elastic constants in the $(SrTiO_3)_n/(PbTiO_3)_n$ superlattices, a spectral iterative perturbation method was employed to solve the mechanical equilibrium equation to obtain the stress field[39]. The pseudocubic lattice constants for $PbTiO_3$ and $SrTiO_3$ were taken as 3.9547 Å and 3.905 Å, respectively[40], while the anisotropic in-plane lattice constants for the substrate $DyScO_3$ is taken from literature to calculate the misfit strain[33]. Material constants for $PbTiO_3$ and $SrTiO_3$ used in the simulations are found in the literature and these include the Landau potentials, elastic constants, electrostrictive coefficients, background dielectric constants, and gradient energy coefficients[37,40–44].

The 3D phase-field simulation of the $(SrTiO_3)_{10}/(PbTiO_3)_{10}$ superlattice was done using discrete grids of $(200\Delta x) \times (200\Delta y) \times (250\Delta z)$ with $\Delta x = \Delta y = \Delta z = 0.4$ nm, where Δx, Δy, and Δz are in real space. The thickness of the substrate, film, and air are $(30\Delta z)$, $(198\Delta z)$, and $(22\Delta z)$, respectively. In the film, alternating n grids of $PbTiO_3$ layers and n grids of $SrTiO_3$ layers are incorporated to simulate the periodically layered superlattice, where n is the superlattice periodicity (for example, $n = 10$ for the 10×10 superlattice). Periodic boundary conditions are assumed in both the x and y directions, and a superposition method is used along the z direction[37]. Random noise is used as the initial setup to simulate the thermal fluctuation during the annealing process.

Using this approach, the 3D phase-field simulation was carried out for a $(SrTiO_3)_{10}/(PbTiO_3)_{10}$ superlattice, and the results are shown in Fig. 4. The vortex–antivortex pairs extending along $DyScO_3$ $[010]_{pc}$ are highlighted in Fig. 4 by red and blue colours having opposite vorticity. The long-range ordering of these vortex pairs along $DyScO_3$ $[100]_{pc}$ in a 10×10 superlattice can be clearly seen in Extended Data Fig. 5c; a subsection shows a vortex–antivortex pair in Extended Data Fig. 5d, which is also shown in Fig. 2d.

A comparison of phase-field models for $n = 10$ and $n = 50$ $PbTiO_3$ thickness highlights the difference between the vortex and flux-closure domain structure (Extended Data Fig. 7). In a true vortex state, polarization is continuously changing about a vortex core giving rise to an inhomogeneous polarization distribution. Such a polarization state is demonstrated using both HR-STEM displacement vector mapping (Extended Data Fig. 7a) and phase-field simulations (Extended Data Fig. 7b) for a 10×10 superlattice. In a flux-closure domain (Extended Data Fig. 7d, e), on the other hand, regions of homogeneous polarization (with a net polarization) can be identified, which are separated by domain walls, giving rise to a polarization distribution similar to those previously observed in bulk materials[18]. In ref. 18, free-standing single crystal lamellae of $BaTiO_3$ were probed using piezoresponse force microscopy, and the results show formation of flux-closure domains, at the length scale of micrometres, which are very similar to the domain pattern reported in ref. 19.

Phase-field calculations were further employed to complete a phase diagram of the evolution of vortex states in these superlattices (that is, total energy density as a function of superlattice periodicity; Extended Data Fig. 8). At lower periodicities ($<10 \times 10$), calculations predict the existence of ferroelastic domains, shown as a_1/a_2 by solid squares. a_1/a_2-type domain structure have domains which are polarized along the in-plane directions (the directions along which mechanical constraints are applied, in this case along $[100]_{pc}$ and $[010]_{pc}$), and are separated by 90° domain walls, making them ferroelastic in nature[45]. After reaching a critical periodicity (~10×10), total energy calculations show that the vortex structure becomes more favourable as compared to the a_1/a_2. Upon transitioning to larger superlattice periods ($>27 \times 27$), the polarization state is stabilized by incorporating flux-closure-type domains, where regions of homogeneous polarization exist, and are separated by domain walls.

Sample size. No statistical methods were used to predetermine sample size.

31. Kuroiwa, Y., Aoyagi, S. & Sawada, A. Evidence of Pb-O covalency in tetragonal $PbTiO_3$. *Phys. Rev. Lett.* **87,** 217601 (2001).
32. Jones, C. W., Battle, P. D., Lightfoot, P. & Harrison, T. A. The structure of $SrRuO_3$ by time-of-flight neutron powder diffraction. *Acta Crystallogr. C* **45,** 365–367 (1989).
33. Chen, Z. H., Damodaran, A. R., Xu, R., Lee, S. & Martin, L. W. Effect of "symmetry mismatch" on the domain structure of rhombohedral $BiFeO_3$ thin films. *Appl. Phys. Lett.* **104,** 182908 (2014).
34. Ophus, C., Nelson, C. T. & Ciston, J. Correcting nonlinear drift distortion of scanning probe microscopy from image pairs with orthogonal scan directions. *Ultramicroscopy* **162,** 1–9 (2016).
35. Glazer, A. M. & Mabud, S. A. Powder profile refinement of lead zirconium titanate at several temperatures. II. $PbTiO_3$. *Acta Crystallogr. B* **34,** 1065–1070 (1978).
36. Chen, L.-Q. Phase-field model of phase transitions/domain structures in ferroelectric thin films: a review. *J. Am. Ceram. Soc.* **91,** 1835–1844 (2008).
37. Li, Y. L., Hu, S. Y., Liu, Z. K. & Chen, L.-Q. Effect of substrate constraint on the stability and evolution of ferroelectric domain structures in thin films. *Acta Mater.* **50,** 395–411 (2002).
38. Li, Y. L., Hu, S. Y., Liu, Z. K. & Chen, L.-Q. Effect of electrical boundary conditions on ferroelectric domain structures in thin films. *Appl. Phys. Lett.* **81,** 427–429 (2002).
39. Wang, J. J., Ma, X. Q., Li, Q., Britson, J. & Chen, L.-Q. Phase transitions and domain structures of ferroelectric nanoparticles: phase field model incorporating strong elastic and dielectric inhomogeneity. *Acta Mater.* **61,** 7591–7603 (2013).
40. Haun, M. J., Furman, E., Jiang, S. J., Mckinstry, H. A. & Cross, L. E. Thermodynamic theory of $PbTiO_3$. *J. Appl. Phys.* **62,** 3331–3338 (1987).
41. Sheng, G. *et al.* A modified Landau-Devonshire thermodynamic potential for strontium titanate. *Appl. Phys. Lett.* **96,** 232902 (2010).
42. Tagantsev, A. K. Landau expansion for ferroelectrics: which variable to use? *Ferroelectrics* **375,** 19–27 (2008).
43. Tagantsev, A. K. The role of background dielectric susceptibility in uniaxial ferroelectrics. *Ferroelectrics* **69,** 321–323 (1986).
44. Zheng, Y. & Woo, C. H. Giant piezoelectric resistance in ferroelectric tunnel junctions. *Nanotechnology* **20,** 075401 (2009).
45. Pompe, W., Gong, X., Suo, Z. & Speck, J. S. Elastic energy release due to domain formation in the strained epitaxy of ferroelectric and ferroelastic films. *J. Appl. Phys.* **74,** 6012–6019 (1993).

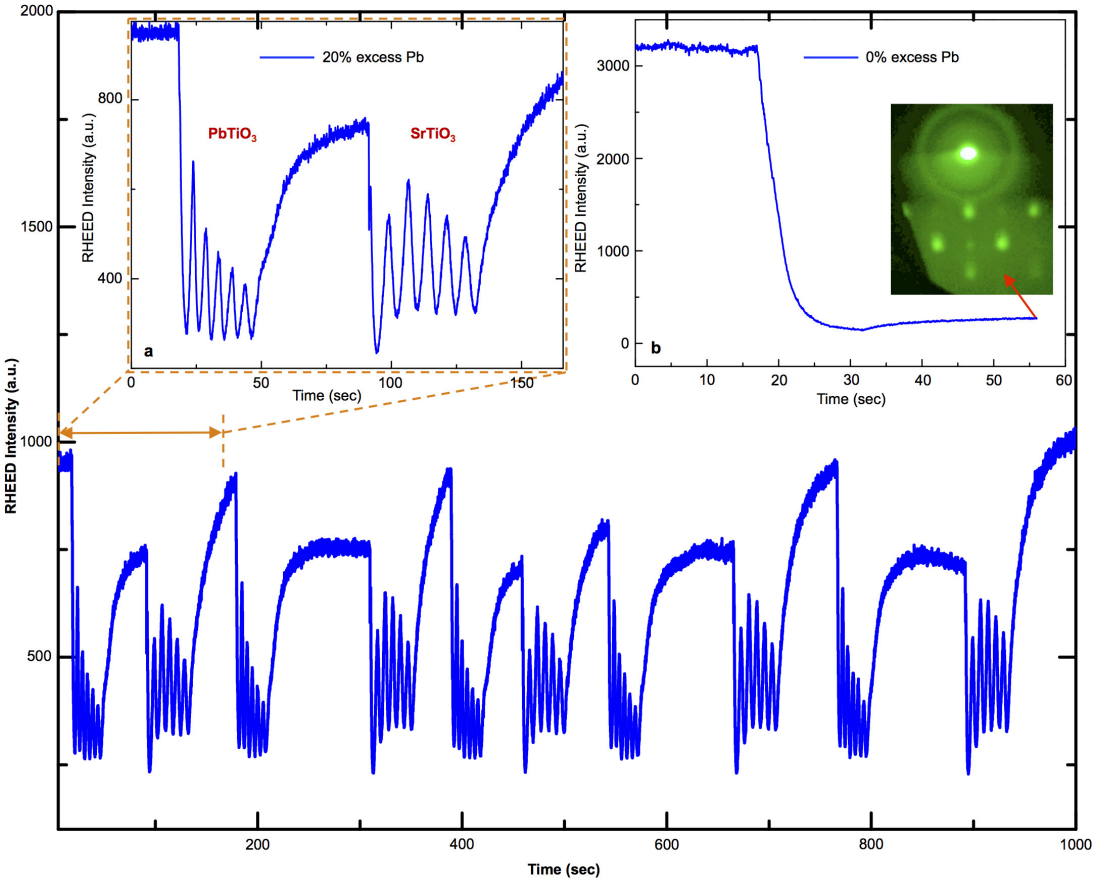

Extended Data Figure 1 | RHEED-controlled growth of superlattices. RHEED oscillations for five periods of a $(SrTiO_3)_6/(PbTiO_3)_6$ superlattice grown using a 20% excess Pb target are shown. The oscillations were present throughout the growth of the 100-nm-thick superlattice. **a**, RHEED oscillations for six unit cells of $PbTiO_3$, followed by oscillations for six unit cells of $SrTiO_3$, that is, one 6×6 superlattice period. **b**, RHEED intensity variation for growth of $PbTiO_3$ from a stoichiometric $PbTiO_3$ or 0% Pb excess target. Inset, RHEED diffraction pattern obtained at the end of growth, highlighting the rapid transition to 3D growth mode when a stoichiometric target is used (Methods).

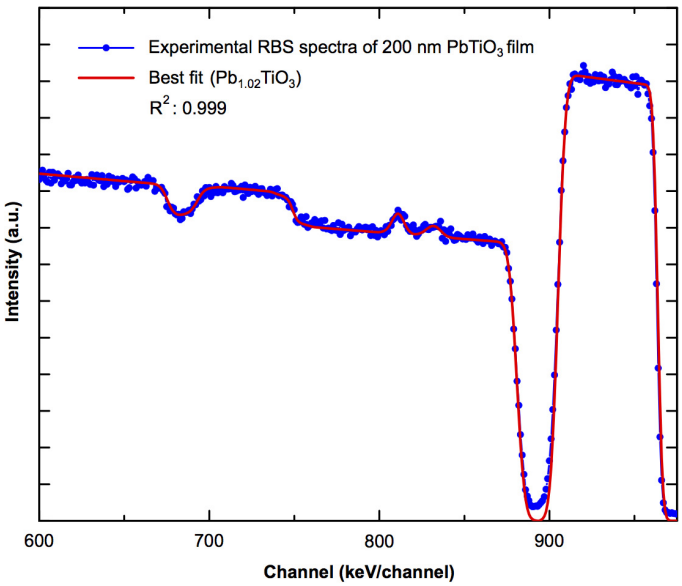

Extended Data Figure 2 | Rutherford backscattering spectrometry (RBS) characterization. An RBS spectrum of a 200-nm $PbTiO_3$ film grown on a single-crystalline $GdScO_3(001)_{pc}$ substrate is shown, along with the simulated spectrum (indicated by 'Best fit' in the figure) for the same structure, revealing an effective Pb:Ti ratio of 1.02:1, which is very close to ideal stoichiometry.

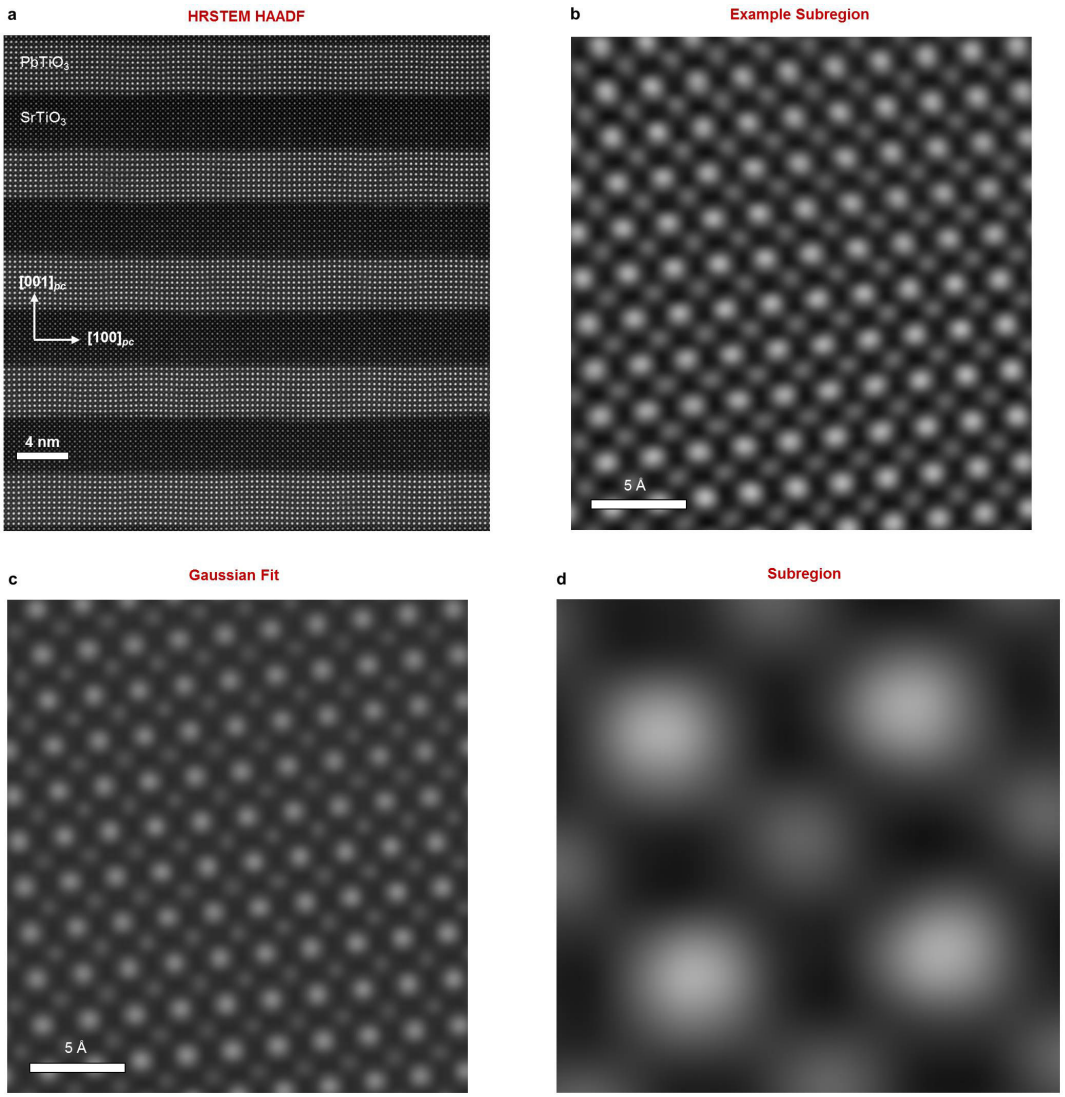

Extended Data Figure 3 | Fitting atomic positions in the HR-STEM images. a, An HR-STEM HAADF image of a $(SrTiO_3)_{10}/(PbTiO_3)_{10}$ superlattice. Polar displacement vectors ($\boldsymbol{P}_{PD}$) are calculated by first finding atom positions by fits of 2D Gaussians to the image intensity. **b**, An example subregion from an HR-STEM image (unrotated). **c**, The corresponding Gaussian fit of **b**. **d**, An example of the B-site-centred five-atom clusters which are fitted simultaneously.

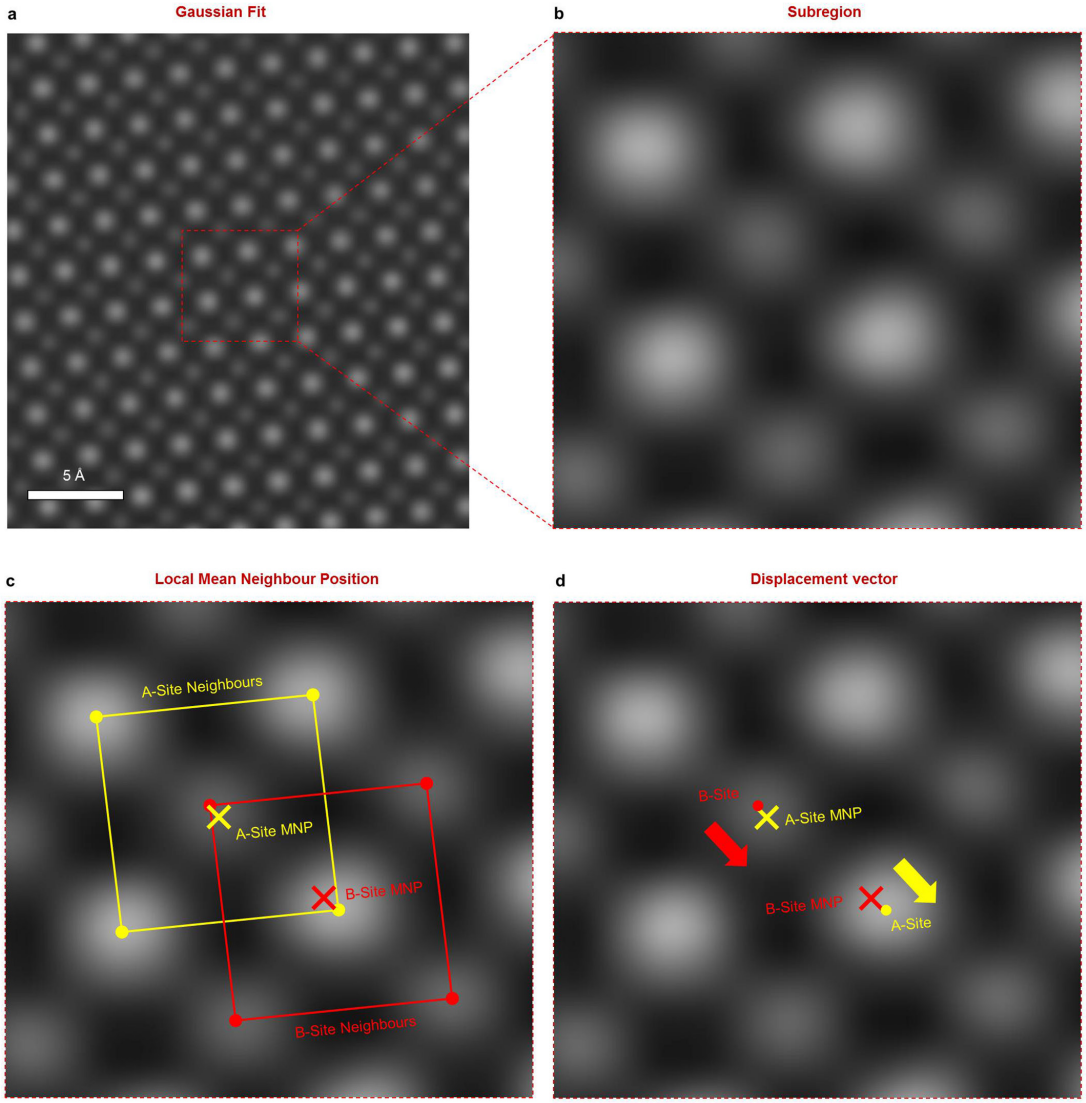

Extended Data Figure 4 | Extracting polar displacement vectors (P_{PD}) from HR-STEM data. a, The Gaussian fit of a region of an HAADF STEM image. **b**, A magnified view of the boxed subregion in **a**, showing two overlapping unit cells, namely, the A-site-centred perovskite unit cell, and the B-site-centred perovskite unit cell. **c**, The mean position of each atom's four nearest cation neighbours (MNP, mean neighbour position) is used to determine a relative sublattice offset. **d**, A polar displacement vector (yellow arrow for A-site and red arrow for B-site), taken as the difference between each atom (filled circle) and the MNP ('×'), is given opposite sign for A- and B-sites to maintain a consistent direction.

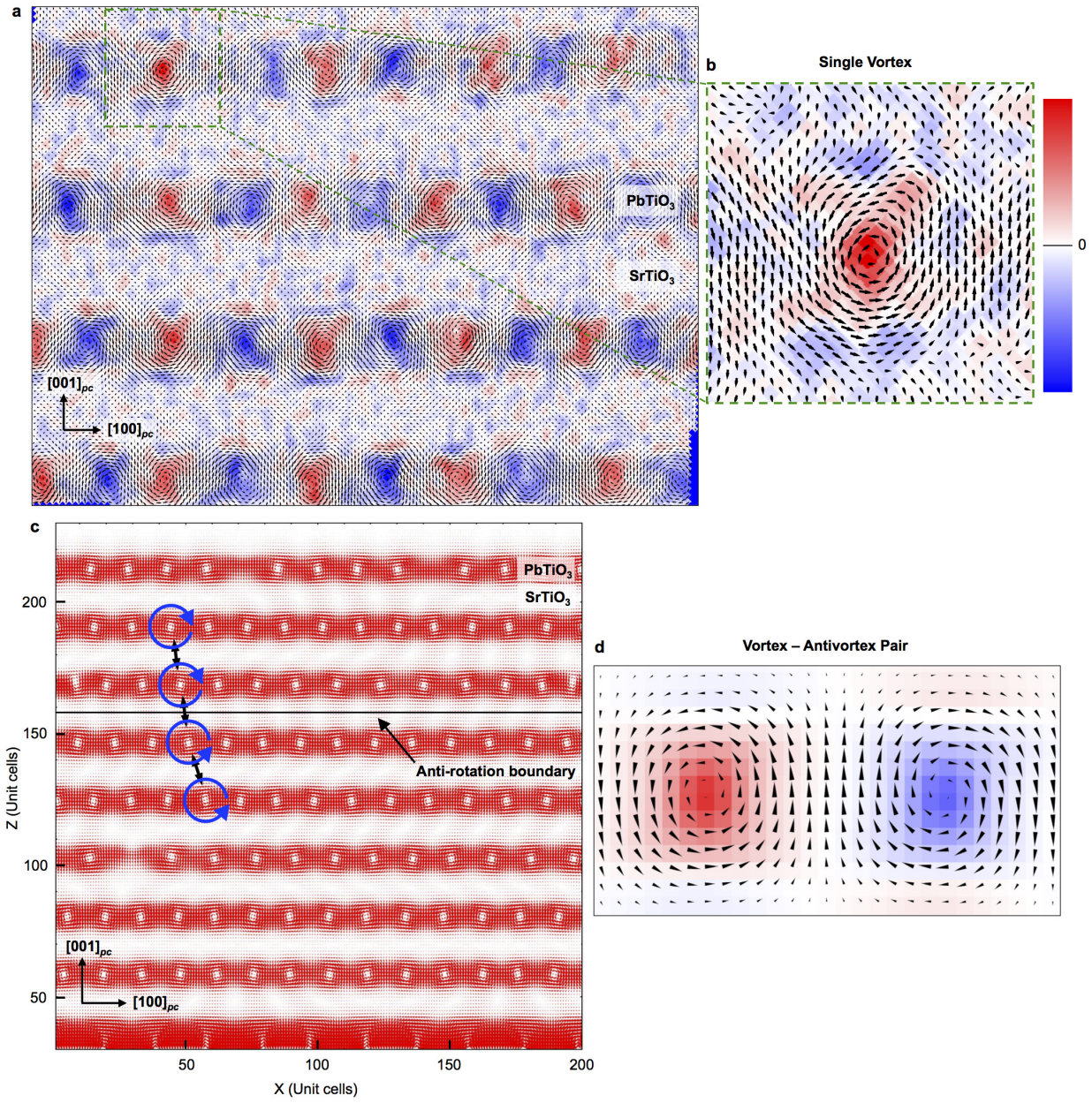

Extended Data Figure 5 | Polar displacement vector map and phase-field simulation of a $(SrTiO_3)_{10}/(PbTiO_3)_{10}$ superlattice. a, The polar displacement vector map (black arrows) corresponding to the $(SrTiO_3)_{10}/(PbTiO_3)_{10}$ superlattice in Fig. 2a is shown overlaid on the colourized $(\nabla \times \boldsymbol{P}_{PD})_{[010]}$. **b**, A magnified view of the highlighted polar vortex shows the smooth rotation increasing towards a vortex core. The extremes of the colour scale of the curl vector are $-16.75\,pm\,nm^{-1}$ and $16.75\,pm\,nm^{-1}$, with blue and red colours indicating negative and positive values of curl (units for polar displacement are in pm). **c**, A cross-section of the phase-field simulation for the $(SrTiO_3)_{10}/(PbTiO_3)_{10}$ superlattice showing the polarization vectors (red arrows) with interlayer alignment. This sample exhibits preference for alignment of matched rotations (indicated by blue arrows), but a phase shift of anti-alignment is also found (indicated by 'Anti-rotation boundary' in the figure). Such defects are found occasionally. **d**, A subregion of the simulation, highlighting a vortex–antivortex pair with the curl of the polarization overlaid.

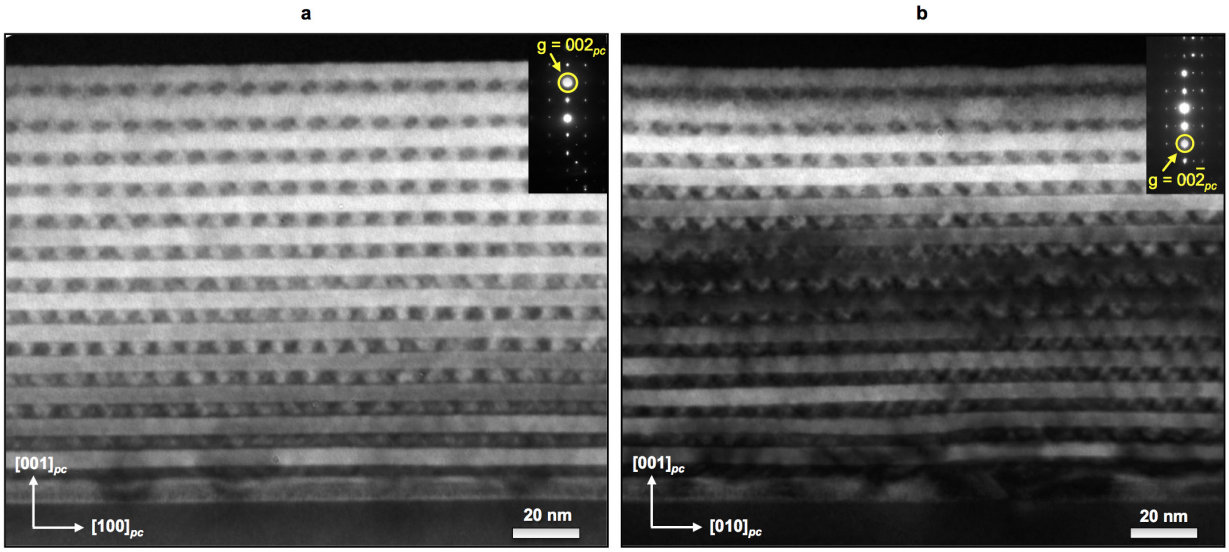

Extended Data Figure 6 | Vortex–antivortex arrays along both pseudo-cubic in-plane directions. a, Cross-sectional DF-TEM of a $(SrTiO_3)_{10}/(PbTiO_3)_{10}$ superlattice taken along the $[010]_{pc}$ zone axis (inset shows the SAED pattern and the *g*-vector for image formation). **b**, Cross-sectional DF-TEM of the same $(SrTiO_3)_{10}/(PbTiO_3)_{10}$ superlattice sample taken along the orthogonal $[100]_{pc}$ zone axis (inset as **a**). In both cases, clear vortex–antivortex structures are observed.

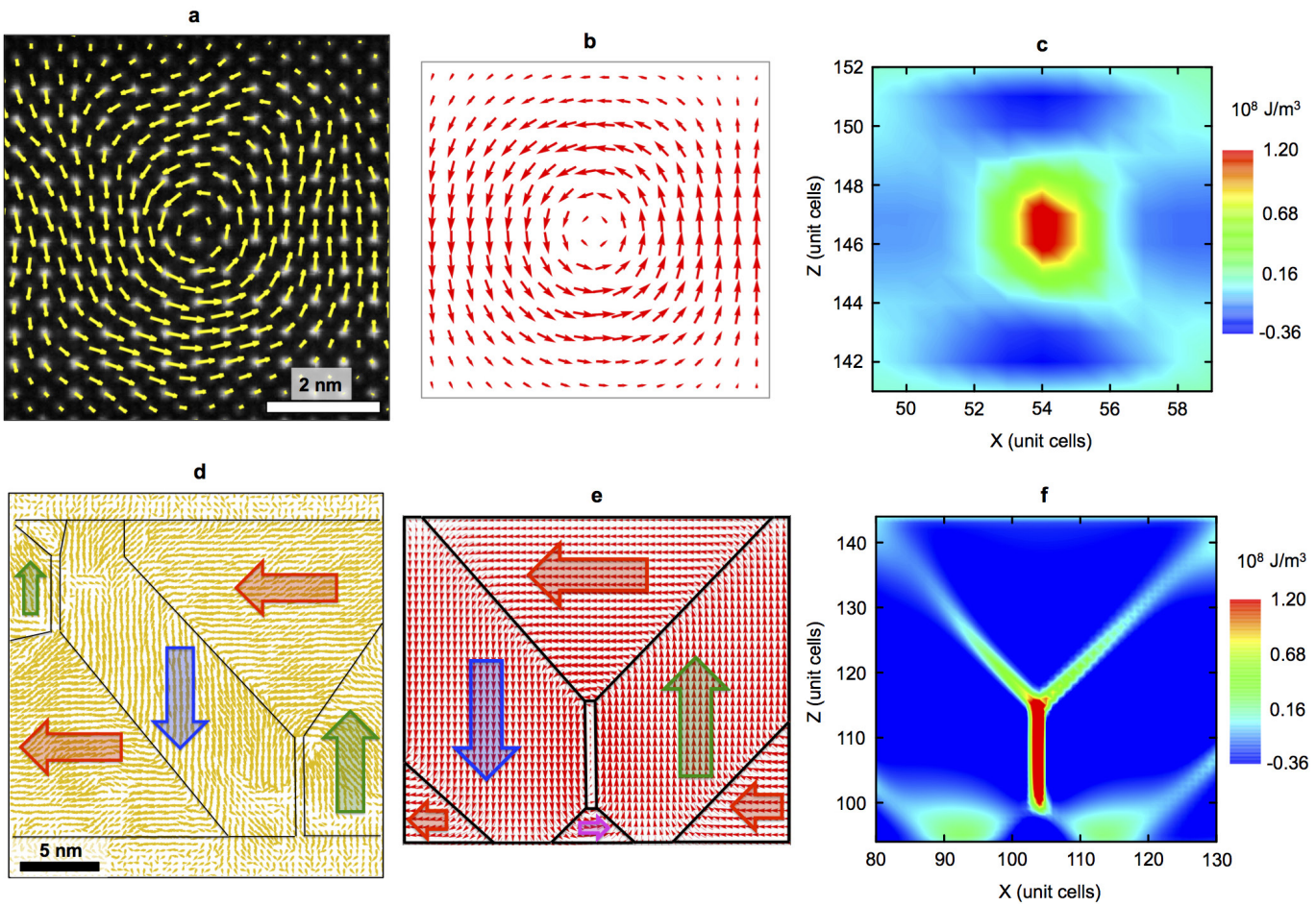

Extended Data Figure 7 | Differentiation of vortex structure from a flux-closure domain structure using phase-field simulations and HR-STEM polar displacement mapping. a, HR-STEM polar displacement vector map of a single vortex in a $(SrTiO_3)_{10}/(PbTiO_3)_{10}$ superlattice. **b**, Phase-field-calculated polarization vector map of a single vortex in a $(SrTiO_3)_{10}/(PbTiO_3)_{10}$ superlattice. **c**, Total energy density variation within a single vortex in a $(SrTiO_3)_{10}/(PbTiO_3)_{10}$ superlattice calculated from phase-field simulations. **d**, HR-STEM polar displacement vector map of a 20-nm $PbTiO_3$ layer in a heterostructure having the same layer stacking as in ref. 19. **e**, Phase-field-calculated polarization vector map of a flux-closure domain in a 20-nm $PbTiO_3$ heterostructure (red, blue, green and pink arrows in **d** and **e** indicate the direction of net polarization within their respective domains). **f**, Total energy density variation within a flux-closure domain calculated using phase-field simulations.

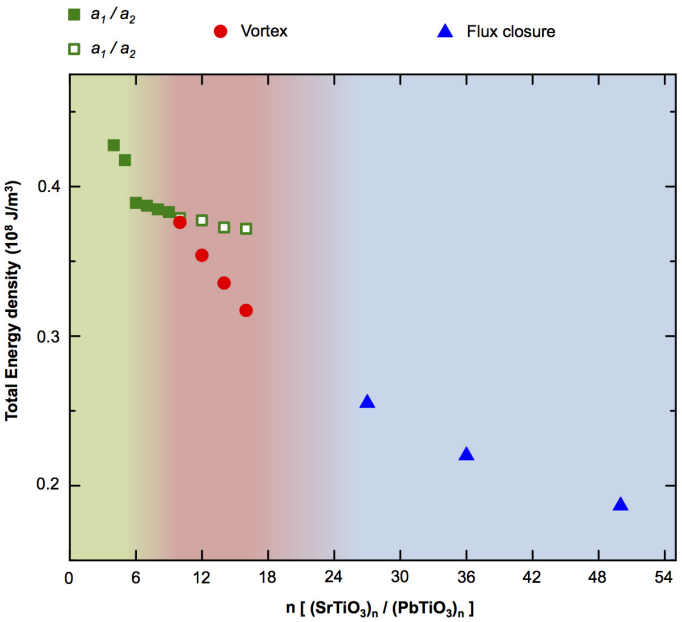

Extended Data Figure 8 | Phase evolution of vortex structure. The phase-field-calculated total energy for various phases competing with a vortex phase is depicted. See Methods for details.

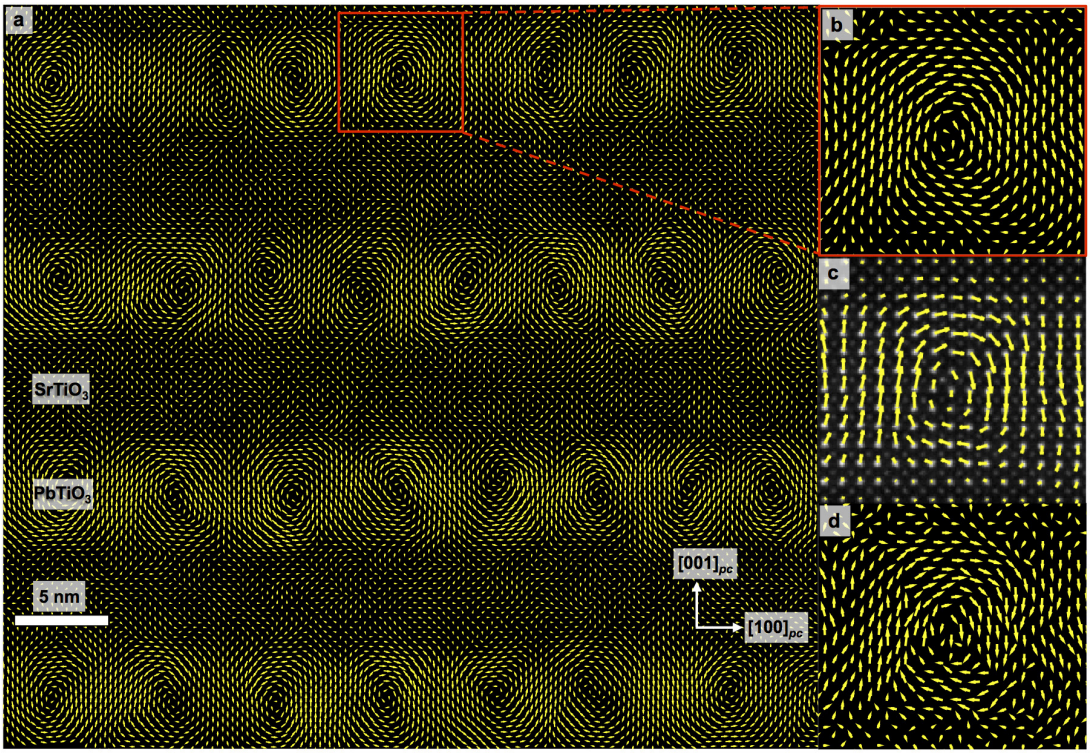

Extended Data Figure 9 | HR-STEM displacement vector map of a $(SrTiO_3)_{10}/(PbTiO_3)_{10}$ superlattice. a, Polar displacement vector map of a $(SrTiO_3)_{10}/(PbTiO_3)_{10}$ superlattice obtained from the same HR-STEM data set as Fig. 2a, showing the polar displacement vectors at all atom positions. **b**, A magnified image of a single vortex. **c**, Polar displacement vector map of the same region as **b**, but plotting only Pb (A-site) centred displacements (like Fig. 2a). **d**, Polar displacement vector map of a single vortex showing the raw displacement vectors.